ACS OMEGA

http://pubs.acs.org/journal/acsodf

Article

Self-Assembly of $Bi_2Sn_2O_7/\beta$-Bi_2O_3 S-Scheme Heterostructures for Efficient Visible-Light-Driven Photocatalytic Degradation of Tetracycline

Baikang Zhu, Qinbin Dong, Jianghua Huang, Mengmeng Yang, Xianlei Chen, Chunyang Zhai, Qingguo Chen, Bohong Wang, Hengcong Tao,* and Li Chen

Cite This: *ACS Omega* 2023, 8, 13702−13714

Read Online

ACCESS | Metrics & More | Article Recommendations | Supporting Information

ABSTRACT: Fabrication of S-scheme heterojunctions with enhanced redox capability offers an effective approach to address environmental remediation. In this study, high-performance $Bi_2Sn_2O_7/\beta$-Bi_2O_3 S-scheme heterojunction photocatalysts were fabricated via the in situ growth of $Bi_2Sn_2O_7$ on β-Bi_2O_3 microspheres. The optimized $Bi_2Sn_2O_7/\beta$-Bi_2O_3 (BSO/BO-0.4) degradation efficiency for tetracycline hydrochloride was 95.5%, which was 2.68-fold higher than that of β-Bi_2O_3. This improvement originated from higher photoelectron−hole pair separation efficiency, more exposed active sites, excellent redox capacity, and efficient generation of $^{\cdot}O_2^-$ and $^{\cdot}OH$. Additionally, $Bi_2Sn_2O_7/\beta$-Bi_2O_3 exhibited good stability against photocatalytic degradation, and the degradation efficiency remained >89.7% after five cycles. The photocatalytic mechanism of $Bi_2Sn_2O_7/\beta$-Bi_2O_3 S-scheme heterojunctions was elucidated. In this study, we design and fabricate high-performance heterojunction photocatalysts for environmental remediation using S-scheme photocatalysts.

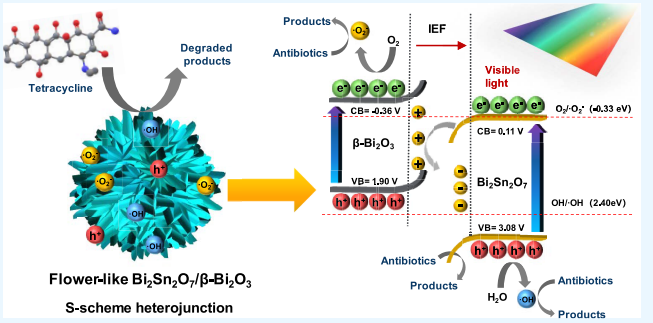

INTRODUCTION

Broad-spectrum antibiotics, such as tetracycline hydrochloride (TC), have been widely used for treating human diseases.[1−3] However, TC is frequently inappropriately disposed in wastewater after its use in animal feeding, human therapy, etc., which severely threatens human health[4−6] and the environment. Besides,[7,8] degradation of TC is difficult in a natural environment owing to its high stability and recalcitrance[7,8]; therefore, a highly effective and inexpensive method is needed for eliminating TC. Semiconductor-based photocatalysis has attracted considerable interest as a water treatment method owing to its lower cost, economic feasibility, and environmental friendliness. A major challenge in semiconductor-based photocatalysis is to develop a photocatalyst that absorbs sufficient sunlight[9,10] and separates[11,12] and generates photogenerated carriers effectively.[13−15]

During the past few years, Bi-based photocatalysis has gained popularity in photocatalysis research because it is environmentally friendly, economical, and efficient. In the coordination process, bismuth ligands usually exhibit a +3 valency and bind strongly to the three outermost electrons. Examples of such catalysts include BiOX (X = Cl, Br, and I),[16−19] $Bi_2Sn_2O_7$,[20−22] Bi_2WO_6,[23−26] and Bi_2MoO_6.[27−30] However, the performance of these catalysts is severely limited because of poor photocarrier separation efficiency. Until now, the photocatalytic performance of catalysts has been enhanced by manipulating their morphology, structure, element doping,[31] and heterojunction construction.[32,33]

Metal−organic frameworks (MOFs) are coordination polymers comprising metal ions and organic molecules.[34−38] They are mainly used in catalysis, adsorption, sensing, and other fields because of their high porosity and specific surface area. Among them, Bi-based MOFs have increasingly attracted attention in green chemistry and environmental remediation owing to the large atomic radius of bismuth and the diversity of its coordination environments, which can enable various applications. Bi-based MOFs reported so far include CAU-7,[39] CAU-17,[40] CAU-31,[41] and CAU-35.[42] Although the preparation[40,43] and structural analysis[44−46] of Bi-based MOFs have been primarily studied, their optical properties, adsorption capacity, and photocatalytic properties have remained largely unexplored. Considering the excellent photocatalytic performance of Bi-based catalysts and the advantages of MOFs, Bi-based MOFs can offer excellent performance in photocatalysis.

Received: December 11, 2022
Accepted: March 28, 2023
Published: April 6, 2023

© 2023 The Authors. Published by American Chemical Society

Bi_2O_3, a wide-band gap semiconductor (2.0−3.9 eV) material capable of exhibiting polymorphism, is nontoxic, harmless, and inexpensive. Meanwhile, Bi_2O_3 can respond to ultraviolet light and visible light to produce reactive oxygen species (ROS), thus decomposing pollutants in water. Metastable Bi_2O_3 is extremely easy to transition to a stable state under the condition of temperature change, so it is necessary to improve its stability and prevent phase transition. According to previous reports, the construction of nanocomposites can effectively solve the metastable problem of Bi_2O_3, so its application in practice is tested. Pyrochlore $Bi_2Sn_2O_7$, which is an ordered fluorite-structure oxide, is a promising photocatalyst that can be easily modified and has an adjustable structure, suitable band structure (approximately 2.75 eV), and low cost.[47,48] Because of $Bi_2Sn_2O_7$ disadvantages such as fast recombination[49,50] and low quantum yield,[51,52] its application in environmental remediation is limited. Nevertheless, heterojunctions can overcome the shortcomings of these catalysts. Optimal heterostructures can prevent recombination of photogenerated carriers and decouple oxidation and reduction. However, typical heterojunctions (i.e., type I[53,54] and II[55,56] heterojunctions) possess charge transfer defects, limiting their redox ability.[57] Z-scheme heterojunctions can simulate natural photosynthesis; the valence band (VB) of the reduction photocatalyst (RP) is more likely to transfer electrons to the conduction band (CB) of the oxidation photocatalyst (OP) because of the large redox potential difference. Hence, the redox capacity of the catalyst cannot be substantially enhanced. Yu and co-workers[58] introduced and discussed a new concept of heterojunctions (i.e., S-scheme heterojunctions[59,60]). OPs have a comparatively low VB position and are mainly used for oxidation reactions. Moreover, RPs with a high CB have a strong reduction ability.[61] S-scheme heterojunctions comprise an RP and OP and have a staggered band structure similar to Type II heterojunctions, but their charge transfer is entirely different from that of Type II heterojunctions.[62] As a result of the generated internal electric field (IEF), under the influence of band bending and the Coulomb effect, photogenerated carriers at the CB of OPs are more likely to recombine with the VB of RPs to form a charge transfer pathway driving the S-scheme heterojunctions.[63,64] The reduction capacity of RPs and the oxidation capacity of OPs are retained to the greatest extent, thereby exhibiting strong reduction and oxidation capacities.[65,66]

In this study, a $Bi_2Sn_2O_7/\beta$-Bi_2O_3 S-scheme heterojunction photocatalyst was prepared by a self-assembly method using CAU-17 as a template. Because of the suitable energy band of the catalyst, successful construction of an S-scheme heterojunction generates a built-in electric field on the catalyst surface, considerably improving the separation efficiency of photoexcited electron−hole pairs. Additionally, $Bi_2Sn_2O_7$ has a better photoresponse in both visible and near-infrared regions. The introduction of $Bi_2Sn_2O_7$ increased the light response range of the heterojunction photocatalyst, thereby increasing the transfer speed of photoexcited charge carriers. The obtained $Bi_2Sn_2O_7/\beta$-Bi_2O_3 photocatalyst exhibited excellent photocatalytic degradation performance in the case of tetracycline. Therefore, ROS required for photodegradation can be produced more efficiently. This new heterojunction photocatalyst offers new opportunities for environmental pollution control.

EXPERIMENTAL PROCEDURE

Materials. All chemicals used in this study were analytically pure and were used as received without purification. Bismuth nitrate pentahydrate ($Bi(NO_3)_3{\cdot}5H_2O$, product number: B110811), terephthalic acid (99%, product number: P108506), sodium stannate trihydrate ($Na_2SnO_3{\cdot}3H_2O$, 98%, product number: S122410), *N*,*N*-dimethylformamide (product number: D111999), ethylene glycol (AR, 99.5%, product number: E103323), sodium sulfate anhydrous (AR, 99%, product number: S112268), potassium ferricyanide (AR, 99.5%, product number: P111564), potassium ferrocyanide trihydrate (AR, 99%, product number: P112421), and potassium chloride (AR, 99.5%, product number: P112134). All materials were purchased from Aladdin Reagent Co. Ltd. (China).

Preparation of Photocatalysts. The preparation process of $Bi_2Sn_2O_7/\beta$-Bi_2O_3 is shown in Figure 1.

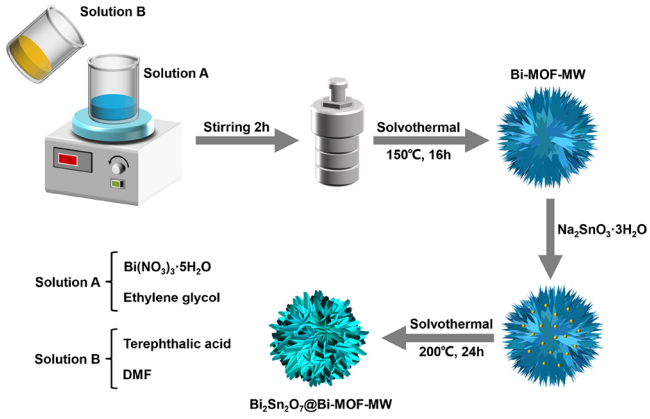

Figure 1. Schematic illustration of the preparation process of CAU-17 and $Bi_2Sn_2O_7/\beta$-Bi_2O_3.

CAU-17 was synthesized using a simple solvothermal self-assembly method. Briefly, 4 mmol of $Bi(NO_3)_3{\cdot}5H_2O$ was dissolved in ethylene glycol (40 mL) for 1 h under ultrasonic conditions to get a solution of A. Meanwhile, 6 mmol of terephthalic acid was dissolved in DMF (30 mL) under magnetic stirring to form a solution of B. Subsequently, the solutions A and B were mixed and stirred continuously for 2 h. The mixed solution was then transferred to a 100 mL Teflon-lined stainless-steel autoclave and heated at 150 °C for 16 h. Upon naturally cooling the autoclave to room temperature, the precipitate was washed six times with ethanol and deionized water and then vacuum-dried overnight at 60 °C.

The preparation method of $Bi_2Sn_2O_7/\beta$-Bi_2O_3 was as follows. First, 0.2 g of CAU-17 was ultrasonically dispersed in 40 mL of ethanol, and *x* mmol of $Na_2SnO_3{\cdot}3H_2O$ was added to 20 mL of deionized water and stirred magnetically. Subsequently, the $Na_2SnO_3{\cdot}3H_2O$ solution was dropped into the CAU-17 suspension and the pH of the suspension was adjusted to pH 13 using 1 M NaOH solution. After stirring for 30 min, the solution was transferred to a 100 mL Teflon-lined stainless-steel autoclave and heated at 200 °C for 24 h; after that, the precipitate was collected, washed, and dried at 60 °C overnight. Subsequently, the dried samples were placed in a Muffle furnace and annealed at 450 °C for 2 h. The samples were labeled BSO/BO-*x*, where *x* represents the molar amount of $Na_2SnO_3{\cdot}3H_2O$ (BSO/BO-0.1, BSO/BO-0.2, BSO/BO-0.3, BSO/BO-0.4, and BSO/BO-0.5).

https://doi.org/10.1021/acsomega.2c07899
ACS Omega 2023, 8, 13702−13714

For comparison, pure $Bi_2Sn_2O_7$ was hydrothermally prepared by substituting $Bi(NO_3)_3{\cdot}5H_2O$ for CAU-17. Moreover, β-Bi_2O_3 was prepared by placing 0.2 g of CAU-17 in a Muffle furnace and annealing it at 450 °C for 2 h.

Characterization. The crystal phase structure of the catalyst was analyzed via X-ray diffraction (XRD, DX-2700, Dandong Fangyuan Instrument Co. Ltd., Dandong, China). The X-ray tube was made of Cu−Pd (λ = 1.5417 Å). The tube voltage and current were 40 kV and 30 mA, respectively. The scan step length and scan range were 0.02° and 5−80°, respectively. The elemental composition and catalyst content were determined via X-ray photoelectron spectroscopy (XPS, Thermo Kalpha, Waltham, USA). The analytical chamber was vacuumed at 8×10^{-10} Pa, the excitation source was Al Ka ray ($h\nu$ = 1486.6 eV) and the operating voltage and the filament current were set at 12.5 kV and 16 mA, respectively. The XPS full spectrum and precision spectra were calibrated using C 1s (284.80 eV). The microstructural characteristics of the catalysts were characterized via scanning electron microscopy (SEM, Zeiss Sigma 300, Zeiss, Oberkochen, Germany). The specific surface areas of the powder samples were calculated from their nitrogen absorption data at 77 K using the Brunauer−Emmett−Teller technique (BET, APSP 2460, Micromeritics, USA). The heat treatment temperature was 200 °C, and the pretreatment time was 6 h. Transmission electron microscopy (TEM, FEI Tecnai F20, FEI, Eindhoven, Netherlands) was performed to obtain high-resolution images using an acceleration voltage of 80−300 kV to analyze the crystal surface of the catalyst. Photoluminescence (PL, FLS1000, Edinburgh, UK) was analyzed using a fluorescence spectrometer (excitation wavelength: 530 nm). Transient photocurrent response (TPR) and electrochemical impedance spectroscopy (EIS) measurements were conducted using a three-electrode electrochemical workstation (CHI660, Chenghua, Shanghai, China). A sodium sulfate anhydrous solution (0.1 M) was used for TPR measurement. A mixed solution of potassium ferricyanide (2.5 mM), potassium ferrocyanide trihydrate (2.5 mM), and potassium chloride (0.1 M) was used as a test solution for EIS measurements.

Photocatalytic Testing. The photocatalytic performance of catalysts for degrading tetracycline (100 mL, 20 mg/L) was measured under visible light (λ > 420 nm), and a 300-W Xe lamp was used as the illumination source (China Education Au-Light Co. Ltd., Beijing). With the assistance of a water-circulating device, the temperature of the photocatalytic system was maintained at 25 °C ± 2 °C. In the experiment, 0.040 g of catalyst was added to a TC solution (100 mL). Subsequently, for adsorption equilibrium, the mixture was ultrasonically treated for 5 min and stirred for 40 min in darkness. The suspension was then continuously stirred under constant agitation under the visible light emitted by the Xe lamp. During this period, 3 mL samples were drawn from the suspension at intervals. The specimen was immediately filtered using a 0.22 μm membrane filter and placed in an ultraviolet (UV) spectrophotometer for determining its absorbance. The detection wavelength was 357 nm.

The specific degradation efficiency (η%) of the catalyst was calculated according to eq 1:

$$\eta\% = (1 - C/C_0) \times 100\% \quad (1)$$

where C_0 represents the initial concentration of the TC solution and C represents the concentration of the TC solution at degradation time t.

Moreover, the reusability of the catalyst was examined by performing cyclic photocatalytic degradation experiments. The photocatalytic process was the same as the aforementioned steps. At the end of each reaction, the catalyst was centrifuged, washed, dried, and then degraded again under identical conditions.

Determination of Reactive Species. In photocatalytic degradation experiments, different free radicals were destroyed by adding different scavengers. Hence, the effects of different free radicals on the TC degradation process were analyzed. Isopropanol (IPA, 0.2 mM), benzoquinone (BQ, 0.2 mM), and ammonium oxalate (AO, 0.2 mM) were used as scavengers to detect $^{\cdot}OH$, $^{\cdot}O_2^-$, and H^+. Further, DMPO-$^{\cdot}O_2^-$ and DMPO-$^{\cdot}OH$ were measured using an electron paramagnetic resonance spectrometer (ESR, BrukerA330, Bruker, Germany).

Detection of Degradation Intermediates. Degradation intermediates were analyzed using the chromatographic column Waters BEH C18 (2.1 × 100 mm, 1.7 μm) in combination with a high-performance liquid chromatography−mass spectroscopy (HPLC−MS) system (Agilent 1290uplc, Agilent QTOF650). A formic acid aqueous solution (0.1%) was used as the mobile phase A, and an acetonitrile solution was used as the mobile phase B; the flow rate was set at 0.3 mL/min. The injection volume of the liquid was 5 μL, and the scanning range was controlled from 5 to 1000 m/z. The sheath gas temperature and flow were set at 350 °C and 12 L/min, respectively.

RESULTS AND DISCUSSION

Compositional, Structural, and Morphological Characterization. Figure 2a shows a strong diffraction peak for

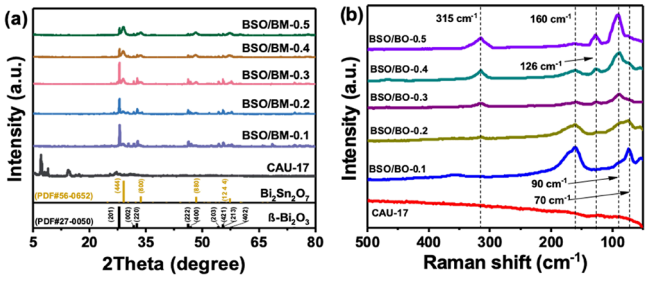

Figure 2. (a) X-ray diffraction (XRD) patterns and (b) Raman spectra of CAU-17 and $Bi_2Sn_2O_7$/β-Bi_2O_3.

CAU-17 at 7.1°, consistent with the literature.[67] Compared with CAU-17, the peak of $Bi_2Sn_2O_7$/β-Bi_2O_3 weakened. The characteristic peaks of $Bi_2Sn_2O_7$/β-Bi_2O_3 at 27.9, 32.7, 46.2, and 55.5° correspond to the (2 0 1), (2 2 0), (2 2 2), and (4 2 1) crystal planes of β-Bi_2O_3 (JCPDS NO.27-0050, Figure S1a).[68,69] The possible reason is that in the process of calcination, the Bi element that did not form $Bi_2Sn_2O_7$ in CAU-17 is converted to β-Bi_2O_3, which makes the diffraction peak of CAU-17 disappear. Further, $Bi_2Sn_2O_7$/β-Bi_2O_3 had a wide peak corresponding to the $Bi_2Sn_2O_7$ (4 4 4) plane at 28.9°, and other characteristic peaks of $Bi_2Sn_2O_7$ appeared at 33.6, 44.1, and 57.2° corresponding to the (8 0 0), (8 8 0), and (12 4 4) planes, respectively (JCPDS No.56-0652, Figure S1b).[70,71] Additionally, with an increase in $Na_2SnO_3{\cdot}3H_2O$ content, the peak intensities of β-Bi_2O_3 (2 0 1) and (2 2 2) planes decreased substantially and the peak intensities of the $Bi_2Sn_2O_7$ (4 4 4) and (8 0 0) planes gradually increased (Figure S2), proving the presence of $Bi_2Sn_2O_7$ and β-Bi_2O_3.

https://doi.org/10.1021/acsomega.2c07899
ACS Omega 2023, 8, 13702−13714

The results showed that $Bi_2Sn_2O_7$ and β-Bi_2O_3 were successfully prepared on the MOFs. A definite existence of $Bi_2Sn_2O_7$ and β-Bi_2O_3 is analyzed using a Raman spectrometer with laser excitation of 785 nm as shown in Figure 2b. Two main peaks at 70 and 96 cm^{-1} correspond to the E_g and A_{1g} phonon modes of rhomboid Bi.[72] The peak values at 126 cm^{-1} correspond to F_{1u} of the Bi−O stretching mode in $Bi_2Sn_2O_7$. The vibration mode of $Bi_2Sn_2O_7$ at 315 cm^{-1} is specified at the F_{2g} mode of Sn−O stretching.[73,74] It can be clearly seen that the Raman peaks of β-Bi_2O_3 are, respectively, located at 160 cm^{-1}, which is consistent with previous reports.[75,76] The results show that the peak strength of β-Bi_2O_3/$Bi_2Sn_2O_7$ composites decreases with the increase of the dosage of $Na_2SnO_3{\cdot}3H_2O$. The results of ICP-OES (Table S1) show that CAU-17 should be completely converted to β-Bi_2O_3. With the increase of $Na_2SnO_3{\cdot}3H_2O$ content, the ratio of Bi element in $Bi_2Sn_2O_7$/β-Bi_2O_3 gradually decreases, while the ratio of Sn element increases. The ratio of β-Bi_2O_3 and $Bi_2Sn_2O_7$ shows an obvious trend, indicating the proportion of catalyst parts.

The morphologies and structures of CAU-17 and BSO/BO-0.4 were observed via SEM, TEM, and high-resolution TEM (HRTEM). Figure 3a,b shows the SEM image of CAU-17. As can be seen from Figure 3a, CAU-17 has a flower-like microspherical morphology (diameter: ∼1.4−1.6 μm) comprising stacked two-dimensional nanorods (Figure 3b).[34] The SEM images of $Bi_2Sn_2O_7$/β-Bi_2O_3 are shown in Figure 3c,d. $Bi_2Sn_2O_7$ was formed on the outer layer of the catalyst, which mainly had a rod-like structure. Additionally, during annealing, Bi without forming $Bi_2Sn_2O_7$ forms β-Bi_2O_3 inside the material and removes impurities, making the rod-like structure on the surface of the sphere protruded. The overall diameter of the prepared composite material was approximately 2.6 μm, and the heterostructure of BSO/BO-0.4 was further confirmed via TEM. The TEM images of BSO/BM-0.4 are shown in Figure 4a,b. BSO/BO-0.4 had a microspherical morphology (Figure 4a), its exterior surface comprised $Bi_2Sn_2O_7$ nanorods extending outward, and the interior of its catalyst comprised β-Bi_2O_3 formed by CAU-17 (Figure 4b). HRTEM showed four distinct interfacial intervals of 0.308, 0.267, 0.188, and 0.161 nm corresponding to (4 4 4), (8 0 0), (8 8 0), and (12 4 4) planes of $Bi_2Sn_2O_7$, respectively (Figure 4c). As can be seen from the element mapping spectrum, Bi and O elements are scattered in the graph. It can be clearly observed through the Sn element that no Sn element exists in the center of the sphere, indicating that the internal material is β-Bi_2O_3. The SEM, TEM, and HRTEM results proved that $Bi_2Sn_2O_7$ was successfully extended on the material's surface. Figure 4d−g shows elemental mapping images of BSO/BO-0.4. In these images, it can be seen from the Bi and Sn elements mapping spectra that β-Bi_2O_3 is mainly concentrated in the lower right part, further indicating the presence of β-Bi_2O_3 in the material and the successful formation of the $Bi_2Sn_2O_7$/β-Bi_2O_3 heterojunction structure.

To detect the chemical states and electronic interactions for β-Bi_2O_3, $Bi_2Sn_2O_7$, and $Bi_2Sn_2O_7$/β-Bi_2O_3, the XPS spectra of β-Bi_2O_3, $Bi_2Sn_2O_7$, and BSO/BO-0.4 were collected; these spectra are shown in Figure S4. Unlike β-Bi_2O_3 and $Bi_2Sn_2O_7$, BSO/BO-0.4 clearly contains Bi, Sn, C, and O, indicating the coexistence of β-Bi_2O_3 and $Bi_2Sn_2O_7$. In Figure 5a, two protruding peaks at 164.55 and 159.25 eV correspond to Bi $4f_{5/2}$ and Bi $4f_{7/2}$, respectively, indicating that Bi exists as Bi^{3+} in BSO/BO-0.4.[77,78] The peaks at 494.50 and 486.05 eV can be attributed to Sn $3d_{3/2}$ and Sn $3d_{5/2}$, respectively, reflecting the presence of Sn^{4+} in BSO/BO-0.4 (Figure 5b).[21,79] In

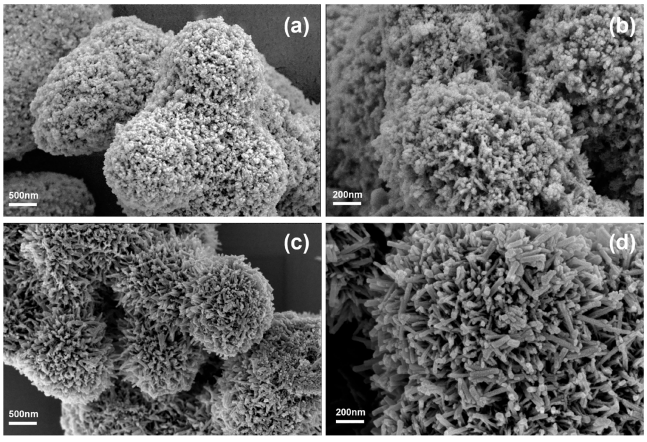

Figure 3. Scanning electron microscopy (SEM) images of (a, b) pristine CAU-17 and (c, d) BSO/BO-0.4.

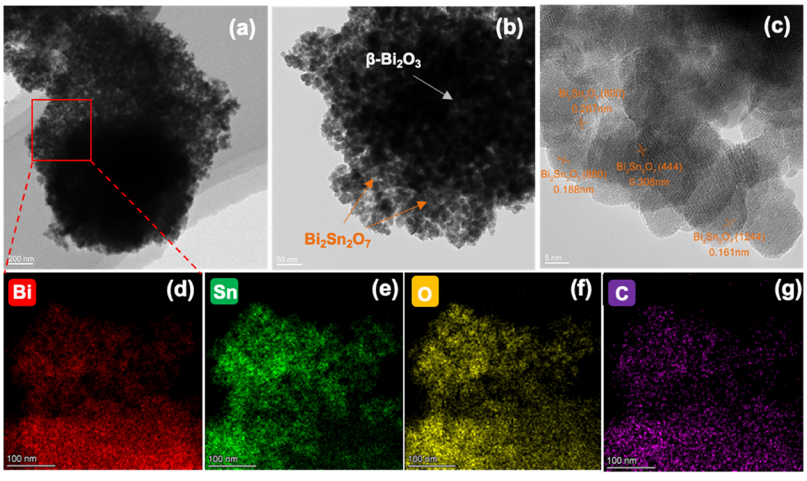

Figure 4. (a, b) Transmission electron microscopy (TEM) images, (c) high-resolution TEM (HRTEM) images and (d−g) elemental mapping of BSO/BO-0.4.

https://doi.org/10.1021/acsomega.2c07899
ACS Omega 2023, 8, 13702−13714

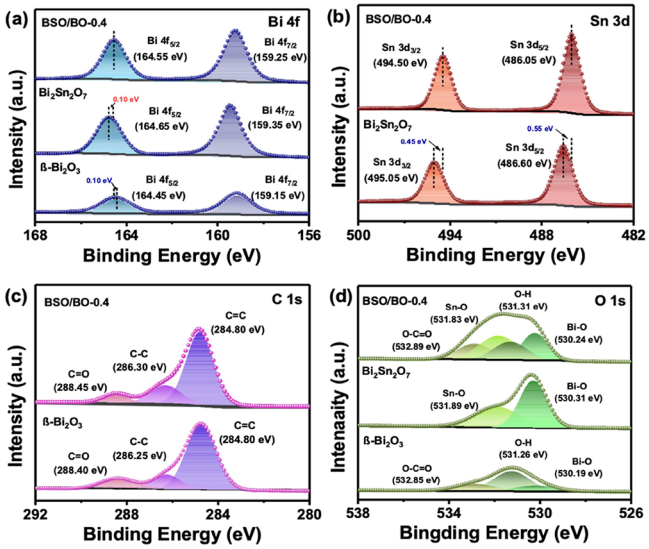

Figure 5. X-ray photoelectron spectroscopy (XPS) spectra of pristine β-Bi_2O_3, $Bi_2Sn_2O_7$, and BSO/BO-0.4: Bi 4f (a), Sn 3d (b), C 1s (c), and O 1s (d).

Figure 5c, 288.45, 286.30, and 284.80 eV are the three peaks of C 1s spectral fitting of BSO/BO-0.4 corresponding to C═O, C−C, and C═C bonds, respectively.[80,81] In Figure 5d, 532.89, 531.83, 531.31, and 530.24 eV are the four peaks of the O 1s spectrum corresponding to O−C═O, Sn−O, O−H, and Bi−O bonds, respectively.[34] Compared with the original β-Bi_2O_3 and $Bi_2Sn_2O_7$, the positive and negative shifts of Bi 4f and O 1s binding energies and the negative shifts of Sn 3d binding energies of β-Bi_2O_3 and $Bi_2Sn_2O_7$ indicate strong electronic interaction rather than physical interaction in the BSO/BO-0.4 heterojunction. It can be inferred that electron transfer occurs from β-Bi_2O_3 to $Bi_2Sn_2O_7$, generating an interfacial electric field and enabling the current carriers of $Bi_2Sn_2O_7$ to migrate smoothly to the β-Bi_2O_3 interface.

Motivated by the hierarchical structure of β-Bi_2O_3, $Bi_2Sn_2O_7$, and BSO/BO-0.4, we analyzed the BET-specific surface area and pore size distribution (Figure 6). Specifically, β-Bi_2O_3

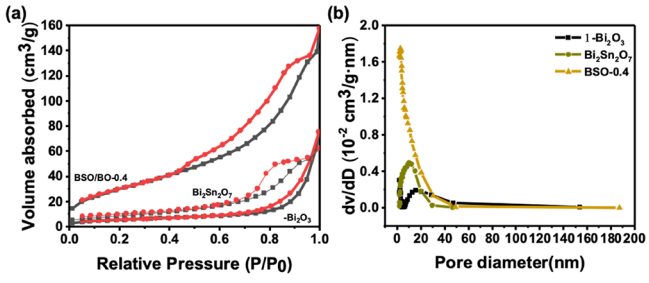

Figure 6. (a) Nitrogen adsorption−desorption isotherms and (b) pore size distribution of β-Bi_2O_3, $Bi_2Sn_2O_7$, and BSO/BO-0.4 heterojunctions.

presents a type III isotherm, and $Bi_2Sn_2O_7$ and BSO/BO-0.4 heterojunction presents a type IV isotherm, and the pore distribution curves further confirmed the presence of mesopores in BSO/BO-0.4. Compared with β-Bi_2O_3 and $Bi_2Sn_2O_7$, BSO/BO-0.4 had a higher BET-specific surface area (113.65 m^2 g^{-1}) compared with original β-Bi_2O_3 (20.01 m^2 g^{-1}) and $Bi_2Sn_2O_7$ (29.80 m^2 g^{-1}) (Table 1). The presence of many mesoporous structures in BSO/BO-0.4 increases the number of reaction sites.

Table 1. S_{BET} and Average Pore Size of Bi-MOF-MW and BSO/BM-0.4 Heterojunctions

sample	S_{BET} (m^2/g)	average pore diameter (nm)
β-Bi_2O_3	20.01	23.20
$Bi_2Sn_2O_7$	29.80	12.97
BSO/BM-0.4	113.65	7.97

Optical and Electronic Properties. UV−visible light (UV−vis) diffuse reflectance spectroscopy (DRS) was performed to characterize the optical properties of β-Bi_2O_3, $Bi_2Sn_2O_7$, and BSO/BO-0.4 (Figure 7a). Specifically, β-Bi_2O_3

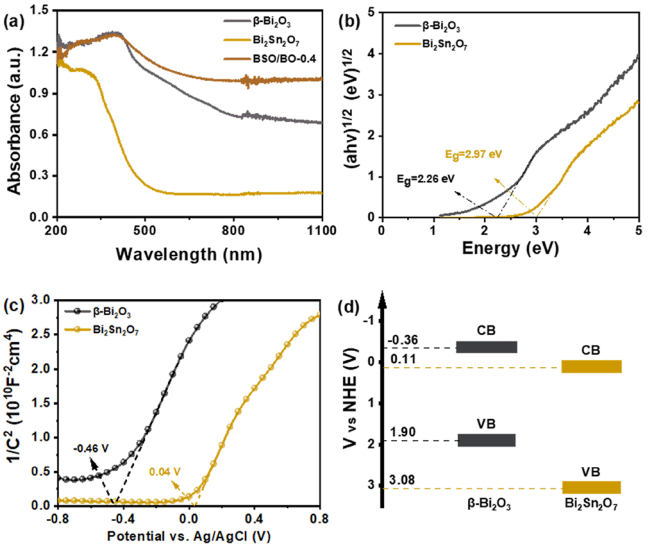

Figure 7. (a) UV−visible light (UV−vis) diffuse reflectance spectroscopy (DRS) of β-Bi_2O_3, $Bi_2Sn_2O_7$, and BSO/BO-0.4; (b) Tauc plots of β-Bi_2O_3 and $Bi_2Sn_2O_7$; (c) Mott−Schottky curves of β-Bi_2O_3 and $Bi_2Sn_2O_7$; and (d) band structure diagrams of β-Bi_2O_3 and $Bi_2Sn_2O_7$.

and $Bi_2Sn_2O_7$ both exhibited excellent visible-light absorption with absorption edges at approximately 615 and 480 nm, respectively.[82,83] BSO/BO-0.4 exhibited enhanced visible-light absorption compared with original β-Bi_2O_3 and $Bi_2Sn_2O_7$, and the introduction of $Bi_2Sn_2O_7$ with a narrow bandgap broadened the absorption range of β-Bi_2O_3, which is conducive to enhancing the photocatalytic performance. The bandgap (E_g) values (Figure 7b) of β-Bi_2O_3 and $Bi_2Sn_2O_7$ were determined using eq 2[84] and were 2.26 and 2.97 eV, respectively.[85]

$$\alpha h\nu = A(h\nu - E_g)^{n/2} \quad (2)$$

To further reveal the redox capacity, Mott−Schottky tests were performed. Particularly, β-Bi_2O_3 and $Bi_2Sn_2O_7$ clearly exhibited n-type semiconductor characteristics (Figure 7c). Additionally, the x-axis intercept was extrapolated to obtain the flat band potential (E_{fb}), and the E_{fb} values of β-Bi_2O_3 and $Bi_2Sn_2O_7$ were determined to be approximately −0.46 and 0.04 V, respectively (vs Ag/AgCl). Because E_{CB} of the n-type semiconductor is approximately 0.1 V higher than that of E_{fb}, the E_{CB} values of β-Bi_2O_3 and $Bi_2Sn_2O_7$ were approximately −0.56 and −0.96 V, respectively (vs Ag/AgCl). According to

https://doi.org/10.1021/acsomega.2c07899
ACS Omega 2023, 8, 13702−13714

eq 3,[86,87] their corresponding E_{NHE} values were determined to be −0.36 and 0.11 V (vs NHE), respectively.

$$E_{NHE} = E_{Ag/AgCl} + 0.197 \quad (3)$$

Hence, the E_{VB} values of β-Bi_2O_3 and $Bi_2Sn_2O_7$ were calculated to be 1.90 and 3.08 V, respectively (vs NHE), according to the Nernst formula (eq 4).

$$E_{CB} = E_{VB} - E_g \quad (4)$$

The band structures of β-Bi_2O_3 and $Bi_2Sn_2O_7$ are shown in Figure 7d.

Photocatalytic Activity. To characterize the photocatalytic activity of the $Bi_2Sn_2O_7/\beta$-Bi_2O_3 heterojunction, the degradation efficiency of degraded pollutants (TC) under visible light was evaluated. The photocatalytic reaction was conducted after 40 min in darkness to achieve adsorption equilibrium. As shown in Figure 8a, the self-degradation effect

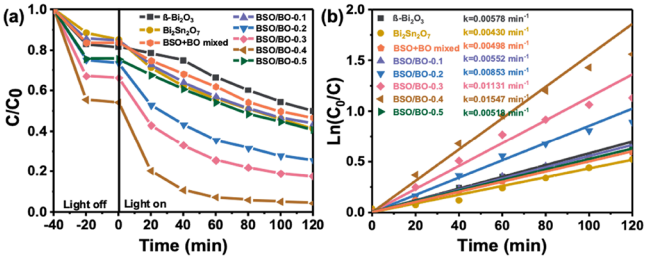

Figure 8. (a) Degradation curves and (b) pseudo-first-order kinetics of β-Bi_2O_3, $Bi_2Sn_2O_7$, and $Bi_2Sn_2O_7/\beta$-Bi_2O_3 (40 mg) for tetracycline (TC) (20 mg/L, 100 mL).

of the TC pollutant solution was almost negligible in the absence of the catalyst. Under visible light, the TC degradation efficiencies of β-Bi_2O_3 and $Bi_2Sn_2O_7$ after 120 min were only 58.6 and 49.9%, respectively, because of severe recombination of photocarriers. Meanwhile, BSO + BO mixed, which uses the physical mixing method to simply stir $Bi_2Sn_2O_7$ and β-Bi_2O_3 and then dry them, does not show a good removal rate in the photocatalytic degradation experiment, and its degradation efficiency is only 53.4%. Interestingly, once $Bi_2Sn_2O_7$ was combined with β-Bi_2O_3, the resulting $Bi_2Sn_2O_7/\beta$-Bi_2O_3 heterojunction exhibited remarkably enhanced photocatalytic degradation efficiency. Among them, BSO/BO-0.4 exhibited the best degradation effect, reaching 95.5% after 120 min of irradiation. However, with increasing $Na_2SnO_3{\cdot}3H_2O$ content, the photocatalytic activity decreased, possibly because of the continuous growth of $Bi_2Sn_2O_7$ leading to the decrease of β-Bi_2O_3 and destruction of charge separation. Therefore, the addition of an appropriate amount of $Na_2SnO_3{\cdot}3H_2O$ facilitates the best synergistic effect between $Bi_2Sn_2O_7$ and β-Bi_2O_3. For comparison, Table 2 lists the TC degradation efficiencies of $Bi_2Sn_2O_7/\beta$-Bi_2O_3 along with those of other heterojunction photocatalysts. Note that $Bi_2Sn_2O_7/\beta$-Bi_2O_3 exhibited higher photocatalytic activity than these photocatalysts, further demonstrating its high catalytic performance. Further, β-Bi_2O_3 exhibited higher adsorption capacity for TC (17.1%) than $Bi_2Sn_2O_7$, but its photocatalytic ability was lower than that of $Bi_2Sn_2O_7$. After $Bi_2Sn_2O_7$ and β-Bi_2O_3 were combined, BSO/BO-0.1, BSO/BO-0.2, BSO/BO-0.3, BSO/BO-0.4, and BSO/BO-0.5 adsorbed 14.4, 24.8, 33.7, 49.8, and 22.3% TC, respectively. The results showed that the adsorption performance of those catalysts improved with an increase in $Bi_2Sn_2O_7$ content. When the ratio of $Bi_2Sn_2O_7$ to β-Bi_2O_3 reached the optimal value (BSO/BO-0.4), the adsorption performance gradually decreased, proving that BSO/BO-0.4 had the largest specific surface area and the smallest average pore size. This could improve its adsorption capacity of the catalyst. Among these heterojunctions, BSO/BO-0.4 exhibited the best adsorption capacity and the highest photocatalytic activity. The results showed that BSO/BO-0.4 had a high pore area and effective separation of photocarriers because of the formation of heterojunctions and proper $Bi_2Sn_2O_7/\beta$-Bi_2O_3 molar ratio, thus achieving high adsorption performance and photocatalytic degradation efficiency. Additionally, the degradation conforms to the pseudo-first-order kinetics according to eq 5:

$$\ln(C_0/C) = kt \quad (5)$$

The degradation curves are shown in Figure 8b. BSO/BO-0.4 had the highest degradation k value (0.01547 min^{-1}) for TC, which is 2.68- and 3.60-fold higher than that of β-Bi_2O_3 (0.00578 min^{-1}) and $Bi_2Sn_2O_7$ (0.00430 min^{-1}).

In addition to catalytic activity, another important indicator for photocatalytic applications is the reusability of the catalyst.[96−98] After five cycles, the photocatalytic performance of BSO/BO-0.4 decreased slightly. However, its degradation efficiency still reached 89.7% (Figure 9a). Figure 9b shows the XRD patterns of fresh and used BSO/BO-0.4. The main peaks of $Bi_2Sn_2O_7$ and β-Bi_2O_3 did not change. Compared with the XRD pattern of BSO/BO-0.4 in Figure 2a, the peak value of the used BSO/BO-0.4 at approximately 27.5° changed, which may be owing to the miscellaneous peaks generated as a result of the preparation process of the catalyst. XPS spectra showed that BSO/BO-0.4 did not change after the reaction (Figure S5). Overall, BSO/BO-0.4 is also suitable for use in visible-light degradation reactions owing to its good reusability.

Table 2. Photocatalytic Degradation of Tetracycline (TC) Using Different Photocatalysts

photocatalysts	light	dosage	TC	degradation	ref
$Bi_2Sn_2O_7$-C_3N_4/Y	400 W halogen lamp	20 mg	20 mg/L, 200 mL	80.4% (90 min)	88
SiO_2/β-Bi_2O_3	300 W-Xe lamp, λ > 420 nm	10 mg	20 mg/L, 50 mL	80.8% (180 min)	89
$SnO_2/Bi_2Sn_2O_7$	300 W-Xe lamp, λ > 420 nm	25 mg	20 mg/L, 50 mL	88.4% (180 min)	90
Bi_2MoO_6/C_3N_5	300 W-Xe lamp, λ > 400 nm	30 mg	20 mg/L, 100 mL	88.1% (75 min)	20
Bi_2MoO_6/CeO_2	300 W-Xe lamp, λ > 420 nm	20 mg	10 mg/L, 50 mL	94.1% (90 min)	91
Bi_2MoO_6/CQDs/Bi_2S_3	300 W-Xe lamp, λ > 420 nm	30 mg	20 mg/L, 100 mL	92.8% (120 min)	92
Ni_2P/Bi_2MoO_6/g-C_3N_4	500 W-Xe lamp, λ > 420 nm	25 mg	20 mg/L, 100 mL	80.1% (120 min)	93
BiOB r/Bi_2WO_6	300 W-Xe lamp, λ > 420 nm	80 mg	20 mg/L, 80 mL	88.06% (120 min)	94
$Bi_2MoO_6/BiFeO_3$	150 W-Xe lamp, λ > 400 nm	50 mg	10 mg/L, 50 mL	93.8% (90 min)	95
$Bi_2Sn_2O_7/\beta$-Bi_2O_3	300 W-Xe lamp, λ > 420 nm	40 mg	20 mg/L, 100 mL	95.5% (60 min)	this work

https://doi.org/10.1021/acsomega.2c07899
ACS Omega 2023, 8, 13702−13714

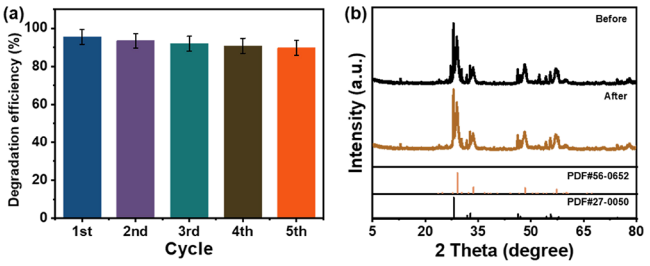

Figure 9. (a) Recycling performance of BSO/BO-0.4 for tetracycline (TC) degradation and (b) X-ray diffraction (XRD) patterns of the fresh and used BSO/BO-0.4.

Degradation Pathways of TC. To better understand the TC degradation process induced by the BSO/BO-0.4 heterojunction, the HPLC−MS system was used for detecting the intermediates by degrading TC (Figure S6); the detected degradation intermediates are listed in Table S2. Previous studies have shown that electron-donating groups and ionizable groups are susceptible to radical attack.[99] Figure 10a shows the main degradation pathways of TC on BSO/BO-0.4. In Pathway 1, owing to the unstable C═C double bond, P1 (m/z = 461) is formed via the hydroxylation reaction[100] and P2 (m/z = 433) is further formed. Upon losing its amide group, P2 further converts to P3 (m/z = 388). Next, P4 (m/z = 338) is formed because of deamination and a ring-opening reaction, and the subsequent dehydroxylation reaction generates P5 (m/z = 307).[101] In Pathway 2, P6 (m/z = 427) results from the absence of OH in the parent molecule. Meanwhile, P7 (m/z = 431) is produced through methylation. P8 (m/z = 417) is formed because of the loss of the methyl group when the $^{\cdot}O_2^-$ free radical attacks saturated the N atom.[102] Subsequently, this is followed by the loss of the amide group to form P9 (m/z = 373) and the detachment of the hydroxyl and amino groups from P9 to P10 (m/z = 342). Because of the strong oxidation capacity of $^{\cdot}OH$, P10 undergoes a ring-splitting reaction to form P11 (m/z = 318), which is then converted to P12 (m/z = 274).[103,104] P10 can also form P5 through ring-opening reactions and methylation processes. Pathway 3 is transformed from P8 to P13 (m/z = 362) via demethylation and deamidation; subsequently, P14 (m/z = 326) is obtained via hydroxyl division. Meanwhile, P13 can also be converted to P4 through a ring-opening reaction. Upon reactive species attacks, these degradation intermediates are finally broken down and mineralized into small molecules.

Photocatalytic Degradation Mechanism. To further demonstrate that the S-scheme heterojunction formed by $Bi_2Sn_2O_7/\beta$-Bi_2O_3, the separation behavior of carriers in the $Bi_2Sn_2O_7/\beta$-Bi_2O_3 photocatalyst was investigated via PL, TPR, and EIS analyses (Figure 11). Figure 11a shows the PL spectra

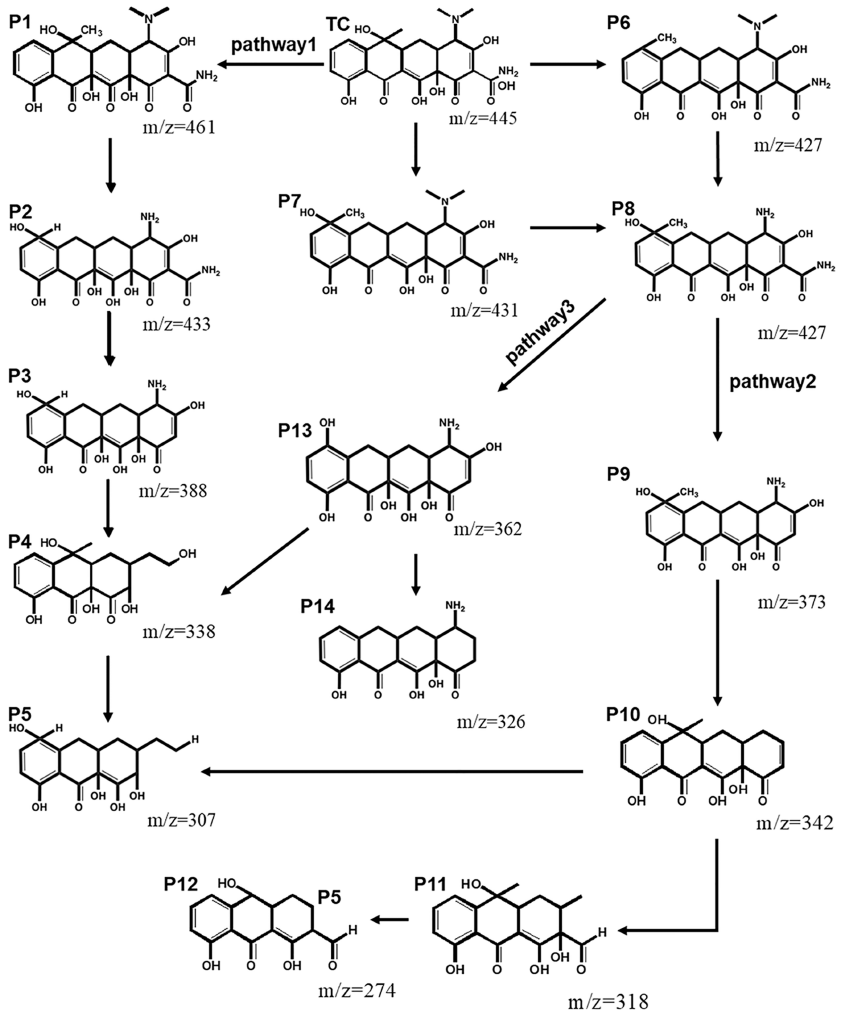

Figure 10. Possible photodegradation pathways of BSO/BO-0.4 for tetracycline (TC).

https://doi.org/10.1021/acsomega.2c07899
ACS Omega 2023, 8, 13702−13714

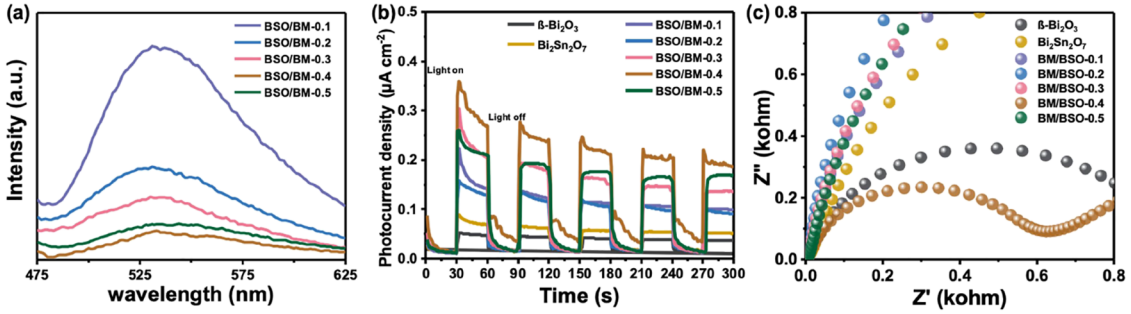

Figure 11. Photoluminescence (PL) spectra (a), transient photocurrent response (TPR) (b), and electrochemical impedance spectroscopy (EIS) (c) of β-Bi_2O_3 and $Bi_2Sn_2O_7$ and $Bi_2Sn_2O_7$/β-Bi_2O_3 heterojunctions.

of the $Bi_2Sn_2O_7$/β-Bi_2O_3 heterojunction (excitation wavelength [λ_{ex}]: 530 nm). Semiconductors with higher PL emissions can recombine more photocarriers in general.[105−107] BSO/BO-0.4 had a lower quenching PL emission intensity than $Bi_2Sn_2O_7$ and β-Bi_2O_3, which indicates that construction of the $Bi_2Sn_2O_7$/β-Bi_2O_3 heterojunction hinders the recombination of the photogenerated carriers, ensuring that the photogenerated carriers last longer and that interfacial charge transfer is more efficient. Thus, the photocatalytic performance of the $Bi_2Sn_2O_7$/β-Bi_2O_3 heterojunction could be improved (notably, BSO/BO-0.4 had the lowest PL emission intensity).

To gain a better understanding of photoinduced carrier transfer and separation, the TPR spectra of $Bi_2Sn_2O_7$, β-Bi_2O_3, and $Bi_2Sn_2O_7$/β-Bi_2O_3 heterojunctions were recorded (Figure 11b). The $Bi_2Sn_2O_7$/β-Bi_2O_3 heterojunction showed good photocurrent reproducibility, i.e., it was highly stable under illumination and in darkness. Among all catalysts, the lowest electron−hole compound efficiency (corresponding to the highest photocurrent) was found in BSO/BO-0.4.

To learn more about the carrier migration behavior of the produced samples, EIS spectra were collected (Figure 11c). As can be observed, the charge transfer resistance generally decreases as the semicircle gets smaller. The diameter of the semicircle of BSO/BO-0.4 was the smallest; moreover, the highest charge separation efficiency was observed in BSO/BO-0.4 owing to its lowest interfacial charge transfer resistance (Figure 11c). This result confirmed that the $Bi_2Sn_2O_7$/β-Bi_2O_3 heterojunction can promote interfacial charge transfer and hinder charge recombination, improving photocatalytic performance.

The production of free radicals for TC degradation by $Bi_2Sn_2O_7$/β-Bi_2O_3 was investigated using capture experiments and ESR analysis. Figure S7 shows the free radical capture experiment of $Bi_2Sn_2O_7$/β-Bi_2O_3, BQ, IPA, and AO used as the scavengers of free radicals. In the absence of any scavenger, the degradation efficiency of BSO/BO-0.4 for TC was 95.5%. The introduction of BQ, IPA, and AO reduced the photodegradation efficiency from 95.5% to 56.4, 67.3, and 89.7%, respectively, indicating that $^{\cdot}O_2^-$and $^{\cdot}OH$ were the main active species for TC degradation by BSO/BO-0.4.

The ESR technique was used to analyze the useful free radicals ($^{\cdot}O_2^-$and $^{\cdot}OH$) generated under visible-light conditions. The intensity of the DMPO-$^{\cdot}O_2^-$ signal was detected at 5 min, indicating that $^{\cdot}O_2^-$ free radical could not be generated by bare $Bi_2Sn_2O_7$ (Figure 12a). Interestingly, the DMPO-$^{\cdot}O_2^-$ signal produced on BSO/BO-0.4 was remarkably stronger than that of original β-Bi_2O_3, suggesting that more $^{\cdot}O_2^-$ radicals were produced by BSO/BO-0.4. Further, β-Bi_2O_3

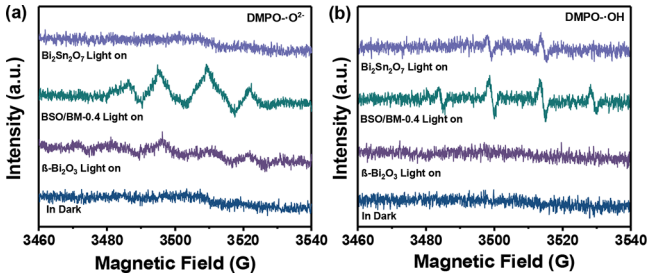

Figure 12. Electron spin resonance (ESR) spin-trapping spectra of β-Bi_2O_3, $Bi_2Sn_2O_7$, and BSO/BO-0.4 for detecting $^{\cdot}O_2^-$ (a) and $^{\cdot}OH$ (b) radicals.

cannot produce $^{\cdot}OH$ radicals owing to the absence of the DMPO-$^{\cdot}OH$ peak. The DMPO-$^{\cdot}OH$ signal produced on BSO/BO-0.4 was also stronger than that of $Bi_2Sn_2O_7$, reflecting the formation of more $^{\cdot}OH$ radicals by BSO/BO-0.4 (Figure 12b). The results showed that $^{\cdot}O_2^-$ and $^{\cdot}OH$ were the main active species of BSO/BO-0.4. The heterostructure formed by BSO/BO-0.4 had a high CB potential and a deep VB potential, which are conducive to the formation of $^{\cdot}O_2^-$ and $^{\cdot}OH$ radicals, verifying its S-scheme heterojunction characteristics.

The S-scheme carrier transfer mechanism of $Bi_2Sn_2O_7$/β-Bi_2O_3 is illustrated in Figure 13. As previously described, the generation of IEF of the catalyst leads to transformation from β-Bi_2O_3 to $Bi_2Sn_2O_7$ at the heterojunction interface, making the energy bands of $Bi_2Sn_2O_7$ bend downward while those of β-Bi_2O_3 bend upward. Therefore, the directional movement of the built-in electric field can maximize the transfer of electrons from $Bi_2Sn_2O_7$ to β-Bi_2O_3.[108,109] Moreover, the electrons of β-Bi_2O_3 (−0.36 V vs NHE) rather than $Bi_2Sn_2O_7$ (+0.11 V vs NHE) can reduce O_2 to form $^{\cdot}O_2^-$ (−0.33 V vs NHE).[110] Nevertheless, because of the higher VB potential of $Bi_2Sn_2O_7$ (3.08 V vs NHE) compared with that of β-Bi_2O_3 (1.90 V vs NHE), the former can oxidize H_2O to produce $^{\cdot}OH$ (2.4 V vs NHE).[111,112] These results are consistent with the results of capture tests and ESR analysis. Therefore, $Bi_2Sn_2O_7$/β-Bi_2O_3 S-scheme heterostructures are activated to produce photogenerated electron−hole pairs under photoexcitation (eq 6), a built-in electric field is formed between the interfaces of the materials and the energy band is bent so that the photoexcited electrons in the CB of $Bi_2Sn_2O_7$ can transfer to the VB of β-Bi_2O_3 and recombine (eq 7).[113] The heterojunction structure between $Bi_2Sn_2O_7$ and β-Bi_2O_3 ensures the occurrence of this process. Therefore, $Bi_2Sn_2O_7$ and β-Bi_2O_3 heterojunction can greatly enhance the efficiency of carrier separation and its catalytic activity, as confirmed by the PL, TPR, and EIS results (Figure 10). More importantly, the CB of β-Bi_2O_3 and the VB

https://doi.org/10.1021/acsomega.2c07899
ACS Omega 2023, 8, 13702−13714

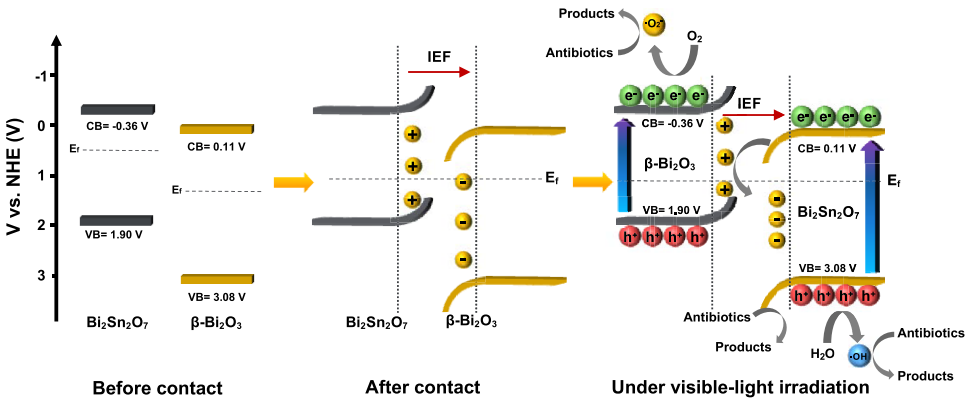

Figure 13. Proposed photocatalytic performance improvement mechanism of the $Bi_2Sn_2O_7/\beta$-Bi_2O_3 S-scheme heterojunction.

of $Bi_2Sn_2O_7$ retain the maximum redox power to generate $\cdot O^{2-}$and $\cdot OH$ radicals owing to the abovementioned recombination of the CB of $Bi_2Sn_2O_7$ and the VB of β-Bi_2O_3, respectively (eqs 8 and 9). Finally, a large number of free radicals (such as $\cdot O_2^-$and $\cdot OH$ species) can attack antibiotics adsorbed on the surface of the $Bi_2Sn_2O_7/\beta$-Bi_2O_3 heterojunction, achieving efficient degradation (eq 10).[114] Overall, S-scheme heterojunctions play a key role in the enhanced photocatalytic performance of $Bi_2Sn_2O_7/\beta$-Bi_2O_3. Consequently, it maintains the best possible redox activity so that it can fully exert its photocatalytic potential.[115]

$$Bi_2Sn_2O_7/\beta - Bi_2O_3 + h\nu \rightarrow Bi_2Sn_2O_7/\beta - Bi_2O_3(e^-, h^+) \quad (6)$$

$$e^-(Bi_2Sn_2O_7) + h^+(\beta - Bi_2O_3) \rightarrow \text{Recombination} \quad (7)$$

$$e^-(\beta - Bi_2O_3) + O_2 \rightarrow \cdot O_2^- \quad (8)$$

$$h^+(Bi_2Sn_2O_7) + H_2O \rightarrow \cdot OH + H^+ \quad (9)$$

$$\cdot O_2^-/\cdot OH/h^+ + TC \rightarrow CO_2 + H_2O + \text{small molecules} \quad (10)$$

CONCLUSIONS

$Bi_2Sn_2O_7/\beta$-Bi_2O_3 S-scheme heterojunctions were synthesized via the in situ growth of $Bi_2Sn_2O_7$ on β-Bi_2O_3 microspheres. The $Bi_2Sn_2O_7/\beta$-Bi_2O_3 heterojunctions showed remarkable photocatalytic performance in the removal of TC under visible light. The S-scheme charge transport mechanism of $Bi_2Sn_2O_7$ and β-Bi_2O_3 at the close contact interface was mainly selected to improve the light response range of $Bi_2Sn_2O_7$ and β-Bi_2O_3, which effectively prevented the coincidence of photogenerated carriers and showed a strong redox ability. Three possible TC degradation pathways were elucidated via HPLC−MS analysis. Finally, the photocatalytic mechanism of the $Bi_2Sn_2O_7/\beta$-Bi_2O_3 S-scheme heterojunctions was proposed based on a free radical capture experiment and ESR analysis. Our study provides a feasible strategy for constructing S-scheme heterostructures for pharmaceutical antibiotic repair and addressing environmental concerns through hierarchical S-scheme heterojunction photocatalysts in the future.

ASSOCIATED CONTENT

Supporting Information

The Supporting Information is available free of charge at https://pubs.acs.org/doi/10.1021/acsomega.2c07899.

Crystal structures and partial magnifications XRD of β-Bi_2O_3 and $Bi_2Sn_2O_7$; SEM image of BSO/BO-0.4; XPS survey spectra of β-Bi_2O_3, $Bi_2Sn_2O_7$, and BSO/BO-0.4. The Mass spectra of TC and its degradation intermediates; Trapping tests; Element proportion (PDF)

AUTHOR INFORMATION

Corresponding Author

Hengcong Tao − *School of Petrochemical Engineering and Environment, Zhejiang Ocean University, Zhoushan 316022, China; National and Local Joint Engineering Research Center of Harbor Oil & Gas Storage and Transportation Technology, Zhoushan 316022, China;* orcid.org/0000-0002-8893-9623; Email: hengcongtao@zjou.edu.cn

Authors

Baikang Zhu − *School of Petrochemical Engineering and Environment, Zhejiang Ocean University, Zhoushan 316022, China; National and Local Joint Engineering Research Center of Harbor Oil & Gas Storage and Transportation Technology, Zhoushan 316022, China*

Qinbin Dong − *School of Petrochemical Engineering and Environment, Zhejiang Ocean University, Zhoushan 316022, China*

Jianghua Huang − *School of Petrochemical Engineering and Environment, Zhejiang Ocean University, Zhoushan 316022, China*

Mengmeng Yang − *School of Petrochemical Engineering and Environment, Zhejiang Ocean University, Zhoushan 316022, China*

Xianlei Chen − *Zhoushan Institute of Calibration and Testing for Quality and Technology Supervision, Zhoushan, Zhejiang 316000, China*

Chunyang Zhai − *School of Materials Science and Chemical Engineering, Ningbo University, Ningbo 315021, China;* orcid.org/0000-0003-0497-0912

Qingguo Chen − *School of Petrochemical Engineering and Environment, Zhejiang Ocean University, Zhoushan 316022, China;* orcid.org/0000-0001-8905-3448

https://doi.org/10.1021/acsomega.2c07899
ACS Omega 2023, 8, 13702−13714

Bohong Wang − *School of Petrochemical Engineering and Environment, Zhejiang Ocean University, Zhoushan 316022, China*

Li Chen − *Department of General Practice, First Medical Center, Chinese PLA General Hospital, Beijing 100036, China*

Complete contact information is available at: https://pubs.acs.org/10.1021/acsomega.2c07899

Author Contributions

B.Z., Q.D., and J.H. contributed equally to this work. B.Z.: Writing—review & editing, Project administration, Funding acquisition. Q.D.: Conceptualization, Methodology, Writing—original draft. J.H.: Visualization, Writing—original draft. M.Y.: Writing—review & editing. X.C.: Writing—review & editing, Validation. C.Z.: Writing—review & editing. Q.C.: Writing—review & editing. B.W.: Writing—review & editing. H.T.: Conceptualization, Methodology, Writing—review & editing, Supervision, Funding acquisition. All authors have read and agreed to the published version of the manuscript.

Notes

The authors declare no competing financial interest.

■ ACKNOWLEDGMENTS

This work was financially supported by: the NSFC-Zhejiang Joint Fund for Integration of Industrialization and Diversification (U1809214); the National Natural Science Foundation of China (No.22005269); the Natural Science Foundation of Zhejiang Province (No.LQ21B030007); the Special Project of Zhejiang Ocean University (2019C21024); Zhejiang Province Public Welfare Technology Research Project (LGF20D060001); Zhejiang Province Public Welfare Technology Research Project (No.LGF22D060003); Science Foundation of Zhejiang Ocean University (11025092122).

■ REFERENCES

(1) Yang, L.; Si, B.; Tan, X.; Xu, J.; Xu, W.; Zhou, L.; Chen, J.; Zhang, Y.; Zhou, X. Valorization of livestock manure for bioenergy production: A perspective on the fates and conversion of antibiotics. *Resour. Conserv. Recycl.* **2022**, *183*, No. 106352.

(2) Li, M.; Wang, P.; Ji, Z.; Zhou, Z.; Xia, Y.; Li, Y.; Zhan, S. Efficient photocatalytic oxygen activation by oxygen-vacancy-rich CeO_2-based heterojunctions: Synergistic effect of photoexcited electrons transfer and oxygen chemisorption. *Appl. Catal., B: Environ.* **2021**, *289*, No. 120020.

(3) Wang, H.; Chen, T.; Chen, D.; Zou, X.; Li, M.; Huang, F.; Sun, F.; Wang, C.; Shu, D.; Liu, H. Sulfurized oolitic hematite as a heterogeneous Fenton-like catalyst for tetracycline antibiotic degradation. *Appl. Catal., B: Environ.* **2020**, *260*, No. 118203.

(4) Zhang, Y.; Cheng, D.; Xie, J.; Zhang, Y.; Wan, Y.; Zhang, Y.; Shi, X. Impacts of farmland application of antibiotic-contaminated manures on the occurrence of antibiotic residues and antibiotic resistance genes in soil: A meta-analysis study. *Chemosphere* **2022**, *300*, No. 134529.

(5) Olatunde, O. C.; Kuvarega, A. T.; Onwudiwe, D. C. Photo enhanced degradation of contaminants of emerging concern in waste water. *Emerg. Contam.* **2020**, *6*, 283−302.

(6) Ma, S.; Zhan, S.; Jia, Y.; Shi, Q.; Zhou, Q. Enhanced disinfection application of Ag-modified g-C_3N_4 composite under visible light. *Appl. Catal., B: Environ.* **2016**, *186*, 77−87.

(7) Leichtweis, J.; Vieira, Y.; Welter, N.; Silvestri, S.; Dotto, G. L.; Carissimi, E. A review of the occurrence, disposal, determination, toxicity and remediation technologies of the tetracycline antibiotic. *Process Saf. Environ. Prot.* **2022**, *160*, 25−40.

(8) Dhandapani, P.; Prakash, A. A.; AlSalhi, M. S.; Maruthamuthu, S.; Devanesan, S.; Rajasekar, A. Ureolytic bacteria mediated synthesis of hairy ZnO nanostructure as photocatalyst for decolorization of dyes. *Mater. Chem. Phys.* **2020**, *243*, No. 122619.

(9) Ma, R.; Sun, J.; Li, D. H.; Wei, J. J. Review of synergistic photo-thermo-catalysis: Mechanisms, materials and applications. *Int. J. Hydrogen Energy* **2020**, *45*, 30288−30324.

(10) Tang, Z.; Gao, H.; Chen, X.; Zhang, Y.; Li, A.; Wang, G. Advanced multifunctional composite phase change materials based on photo-responsive materials. *Nano Energy* **2021**, *80*, No. 105454.

(11) Koe, W. S.; Lee, J. W.; Chong, W. C.; Pang, Y. L.; Sim, L. C. An overview of photocatalytic degradation: photocatalysts, mechanisms, and development of photocatalytic membrane. *Environ. Sci. Pollut. Res.* **2020**, *27*, 2522−2565.

(12) Wang, Z.; Luo, W.; Yan, S.; Feng, J.; Zhao, Z.; Zhu, Y.; Li, Z.; Zou, Z. $BiVO_4$ nano−leaves: Mild synthesis and improved photocatalytic activity for O_2 production under visible light irradiation. *CrystEngComm* **2011**, *13*, 2500−2504.

(13) Khairnar, S. D.; Kulkarni, A. N.; Shinde, S. G.; Marathe, S. D.; Marathe, Y. V.; Dhole, S. D.; Shrivastava, V. S. Synthesis and characterization of 2-D La-doped Bi_2O_3 for photocatalytic degradation of organic dye and pesticide. *J. Photochem. Photobiol.* **2021**, *6*, No. 100030.

(14) Niu, Z.; Yi, S.; Li, C.; Liu, Y.; Pang, Q.; Liu, Z.; Yue, X. Supporting bimetallic sulfide on 3D TiO_2 hollow shells to boost photocatalytic activity. *Chem. Eng. J.* **2020**, *390*, No. 124602.

(15) Han, J.; Zhu, Z.; Li, N.; Chen, D.; Xu, Q.; Li, H.; He, J.; Lu, J. Metalloporphyrin-based D-A type conjugated organic polymer nanotube for efficient photocatalytic degradation. *Appl. Catal., B: Environ.* **2021**, *291*, No. 120108.

(16) Yang, J.; Liang, Y.; Li, K.; Yang, G.; Yin, S. One-step low-temperature synthesis of 0D CeO_2 quantum dots/2D BiOX (X = Cl, Br) nanoplates heterojunctions for highly boosting photo-oxidation and reduction ability. *Appl. Catal., B: Environ.* **2019**, *250*, 17−30.

(17) Raza, A.; Qin, Z.; Ahmad, S. O. A.; Ikram, M.; Li, G. Recent advances in structural tailoring of BiOX-based 2D composites for solar energy harvesting. *J. Environ. Chem. Eng.* **2021**, *9*, No. 106569.

(18) Arumugam, M.; Natarajan, T. S.; Saelee, T.; Praserthdam, S.; Ashokkumar, M.; Praserthdam, P. Recent developments on bismuth oxyhalides (BiOX; X = Cl, Br, I) based ternary nanocomposite photocatalysts for environmental applications. *Chemosphere* **2021**, *282*, No. 131054.

(19) Talreja, N.; Afreen, S.; Ashfaq, M.; Chauhan, D.; Mera, A. C.; Rodríguez, C. A.; Mangalaraja, R. V. Bimetal (Fe/Zn) doped BiOI photocatalyst: An effective photodegradation of tetracycline and bacteria. *Chemosphere* **2021**, *280*, No. 130803.

(20) Li, S.; Wang, C.; Liu, Y.; Cai, M.; Wang, Y.; Zhang, H.; Guo, Y.; Zhao, W.; Wang, Z.; Chen, X. Photocatalytic degradation of tetracycline antibiotic by a novel $Bi_2Sn_2O_7/Bi_2MoO_6$ S-scheme heterojunction: Performance, mechanism insight and toxicity assessment. *Chem. Eng. J.* **2022**, *429*, No. 132519.

(21) Zhang, D.; Yang, Z.; Hao, J.; Zhang, T.; Sun, Q.; Wang, Y. Boosted charge transfer in dual Z-scheme $BiVO_4$@$ZnIn_2S_4/Bi_2Sn_2O_7$ heterojunctions: Towards superior photocatalytic properties for organic pollutant degradation. *Chemosphere* **2021**, *276*, No. 130226.

(22) Heidari, S.; Haghighi, M.; Shabani, M. Sono-photodeposition of Ag over sono-fabricated mesoporous $Bi_2Sn_2O_7$-two dimensional carbon nitride: Type-II plasmonic nano-heterojunction with simulated sunlight-driven elimination of drug. *Chem. Eng. J.* **2020**, *389*, No. 123418.

(23) Koutavarapu, R.; Syed, K.; Pagidi, S.; Jeon, M. Y.; Rao, M. C.; Lee, D.-Y.; Shim, J. An effective CuO/Bi_2WO_6 heterostructured photocatalyst: Analyzing a charge-transfer mechanism for the enhanced visible-light-driven photocatalytic degradation of tetracycline and organic pollutants. *Chemosphere* **2022**, *287*, No. 132015.

(24) Li, X.; Zhang, H.; Du, X.; Wang, S.; Zhang, Q.; Li, H.; Ye, F. Efficient visible-light-driven degradation of tetracycline by a 2D/2D rGO-Bi_2WO_6 heterostructure. *Environ. Res.* **2022**, *212*, No. 113326.

(25) He, Y.; Wang, D.; Li, X.; Fu, Q.; Yin, L.; Yang, Q.; Chen, H. Photocatalytic degradation of tetracycline by metal-organic frameworks modified with Bi_2WO_6 nanosheet under direct sunlight. *Chemosphere* **2021**, *284*, No. 131386.
(26) Zhu, B.; Song, D.; Jia, T.; Sun, W.; Wang, D.; Wang, L.; Guo, J.; Jin, L.; Zhang, L.; Tao, H. Effective Visible Light-Driven Photocatalytic Degradation of Ciprofloxacin over Flower-like Fe3O4/Bi2WO6 Composites. *ACS Omega* **2021**, *6*, 1647−1656.
(27) Li, J.; Wang, B.; Pang, Y.; Sun, M.; Liu, S.; Fang, W.; Chen, L. Fabrication of 0D/1D Bi_2MoO_6/Bi/TiO_2 heterojunction with effective interfaces for boosted visible-light photocatalytic degradation of tetracycline. *Colloids Surf. A Physicochem. Eng. Asp.* **2022**, *638*, No. 128297.
(28) Zhuang, H.; Cao, H.; Zheng, Z.; Lin, L.; Xu, W. Construction of a novel $Zn_3In_2S_6$/Bi_2MoO_6 composite photocatalyst for enhanced photocatalytic tetracycline degradation. *Mater. Lett.* **2022**, *312*, No. 131700.
(29) Sun, M.; Chen, Z.; Yin, Y.; Huang, B.; He, G.; Chen, H. A facile solvothermal syntheses of NiFe layered double hydroxide-Bi_2MoO_6 heterostructure/reduced graphene oxide with efficient photodegradation for tetracycline. *Environ. Res.* **2022**, *204*, No. 112037.
(30) Sun, K.; Zhou, H.; Li, X.; Ma, X.; Zhang, D.; Li, M. The novel 2-dimensional Bi_2MoO_6-Bi_2O_3-Ag_3PO_4 ternary photocatalyst with n-n-p heterojunction for enhanced degradation performance. *J. Alloys Compd.* **2022**, *913*, No. 165119.
(31) Jin, Y.; Li, F.; Li, T.; Xing, X.; Fan, W.; Zhang, L.; Hu, C. Enhanced internal electric field in S-doped BiOBr for intercalation, adsorption and degradation of ciprofloxacin by photoinitiation. *Appl. Catal., B: Environ.* **2022**, *302*, No. 120824.
(32) Lv, X.; Xu, W.; Qin, W.; Li, W. Electron transfer channel in BiOBr/Bi2O3 heterojunction enhanced photocatalytic removal for fluoroquinolone antibiotics. *Colloids Surf. A Physicochem. Eng. Asp.* **2022**, *648*, No. 129353.
(33) Dou, X.; Chen, Y.; Shi, H. CuBi2O4/BiOBr composites promoted PMS activation for the degradation of tetracycline: S-scheme mechanism boosted Cu2+/Cu+ cycle. *Chem. Eng. J.* **2022**, *431*, No. 134054.
(34) Gu, W.; Li, Q.; Zhu, H.; Zou, L. Facile interface engineering of hierarchical flower spherical-like Bi-metal−organic framework microsphere/Bi2MoO6 heterostructure for high-performance visible−light photocatalytic tetracycline hydrochloride degradation. *J. Colloid Interface Sci.* **2022**, *606*, 1998−2010.
(35) Mathew, G.; Daniel, M.; Peramaiah, K.; Ganesh, M.-R.; Neppolian, B. Real-time electrochemical quantification of H_2O_2 in living cancer cells using Bismuth based MOF. *J. Electroanal. Chem.* **2022**, *914*, No. 116255.
(36) Yan, L.; Gopal, A.; Kashif, S.; Hazelton, P.; Lan, M.; Zhang, W.; Chen, X. Metal organic frameworks for antibacterial applications. *Chem. Eng. J.* **2022**, *435*, No. 134975.
(37) Sukatis, F. F.; Wee, S. Y.; Aris, A. Z. Potential of biocompatible calcium-based metal-organic frameworks for the removal of endocrine-disrupting compounds in aqueous environments. *Water Res.* **2022**, *218*, No. 118406.
(38) Liu, X.; Shan, Y.; Zhang, S.; Kong, Q.; Pang, H. Application of metal organic framework in wastewater treatment. *Green Energy Environ.* **2022**, DOI: 10.1016/j.gee.2022.03.005.
(39) Feyand, M.; Mugnaioli, E.; Vermoortele, F.; Bueken, B.; Dieterich, J. M.; Reimer, T.; Kolb, U.; Vos, P. D.; Stock, P. Automated Diffraction Tomography for the Structure Elucidation of Twinned, Sub-micrometer Crystals of a Highly Porous, Catalytically Active Bismuth Metal−Organic Framework. *Angew. Chem., Int. Ed.* **2012**, *51*, 10373−10376.
(40) Inge, A. K.; Koeppen, M.; Su, J.; Feyand, M.; Xu, H.; Zou, X.; O'Keeffe, M.; Stock, N. Unprecedented Topological Complexity in a Metal-Organic Framework Constructed from Simple Building Units. *J. Am. Chem. Soc.* **2016**, *138*, 1970−1976.
(41) Köppen, M.; Meyer, V.; Ångström, J.; Inge, A. K.; Stock, N. Solvent-Dependent Formation of Three New Bi-Metal−Organic Frameworks Using a Tetracarboxylic Acid. *Cryst. Growth Des.* **2018**, *18*, 4060−4067.
(42) Köppen, M.; Beyer, O.; Wuttke, S.; Lüning, U.; Stock, N. Synthesis, functionalisation and post-synthetic modification of bismuth metal−organic frameworks. *Dalton Trans.* **2017**, *46*, 8658−8663.
(43) Gómez-Oliveira, E. P.; Méndez, N.; Iglesias, M.; Gutiérrez-Puebla, E.; Aguirre-Díaz, L. M.; Monge, M. Building a Green, Robust, and Efficient Bi-MOF Heterogeneous Catalyst for the Strecker Reaction of Ketones. *Inorg. Chem.* **2022**, *61*, 7523−7529.
(44) Zhao, C.; Pan, X.; Wang, Z.; Wang, C.-C. 1+1>2: A critical review of MOF/bismuth-based semiconductor composites for boosted photocatalysis. *Chem. Eng. J.* **2021**, *417*, No. 128022.
(45) Zhao, X.; Li, J.; Li, X.; Huo, P.; Shi, W. Design of metal-organic frameworks (MOFs)-based photocatalyst for solar fuel production and photo-degradation of pollutants. *Chin. J. Catal.* **2021**, *42*, 872−903.
(46) Yu, X.; Sun, J.; Zhao, W.; Zhao, S.; Chen, H.; Tao, K.; Hu, Y.; Han, L. MOF-derived Bi(2)O(3)@C microrods as negative electrodes for advanced asymmetric supercapacitors. *RSC Adv.* **2020**, *10*, 14107−14112.
(47) Phu, N. D.; Vu, P. K.; Dung, D. D.; Bich, D. D.; Oanh, L. M.; Hoang, L. H.; Van Hung, N.; Van Hai, P. Temperature-dependent preparation of bismuth pyrostannate $Bi_2Sn_2O_7$ and its photocatalytic characterization. *Mater. Chem. Phys.* **2019**, *221*, 197−202.
(48) Mohamed, M. M.; Ahmed, S. A. Pd-doped β-Bi2O3/Bi2Sn2O7 hybrid nanocomposites for photocatalytic fluorene oxidation: A green approach for the synthesis of fluorenone/fluorenol mixture. *Microporous Mesoporous Mater.* **2015**, *204*, 62−72.
(49) Zhao, X.; Yu, J.; Cui, H.; Wang, T. Preparation of direct Z-scheme Bi2Sn2O7/g-C3N4 composite with enhanced photocatalytic performance. *J. Photochem. Photobiol. A Chem.* **2017**, *335*, 130−139.
(50) Xu, W.; Fang, J.; Zhu, X.; Fang, Z.; Cen, C. Fabricaion of improved novel p−n junction BiOI/Bi2Sn2O7 nanocomposite for visible light driven photocatalysis. *Mater. Res. Bull.* **2015**, *72*, 229−234.
(51) Xu, W.; Fang, J.; Chen, Y.; Lu, S.; Zhou, G.; Zhu, X.; Fang, Z. Novel heterostructured Bi2S3/Bi2Sn2O7 with highly visible light photocatalytic activity for the removal of rhodamine B. *Mater. Chem. Phys.* **2015**, *154*, 30−37.
(52) Wu, C.; Shen, Q.; Zheng, S.; Zhang, X.; Sheng, J.; Yang, H. Fabrication of Bi2Sn2O7@MIL-100(Fe) composite photocatalyst with enhanced superoxide-radical-dominated photocatalytic activity for ciprofloxacin degradation. *J. Mol. Struct.* **2022**, *1258*, No. 132657.
(53) Shi, W.; Hao, C.; Shi, Y.; Guo, F.; Tang, Y. Effect of different carbon dots positions on the transfer of photo-induced charges in type I heterojunction for significantly enhanced photocatalytic activity. *Sep. Purif. Technol.* **2023**, *304*, No. 122337.
(54) Cai, W.; Zhang, F.; Wang, Y.; Li, D. A novel I-type 0D/0D ZnS@Cu3P heterojunction for photocatalytic hydrogen evolution. *Inorg. Chem. Commun.* **2021**, *134*, No. 109046.
(55) Song, K.; Zhang, C.; Zhang, Y.; Yu, G.; Zhang, M.; Zhang, Y.; Qiao, L.; Liu, M.; Yin, N.; Zhao, Y.; Tao, Y. Efficient tetracycline degradation under visible light irradiation using CuBi2O4/ZnFe2O4 type II heterojunction photocatalyst based on two spinel oxides. *J. Photochem. Photobiol. A Chem.* **2022**, *433*, No. 114122.
(56) Zhang, Y.; Yan, Y.; Shen, G.; Hong, K. Synthesis of type-II heterojunction films between ReS2 and XS2 (X = Mo,W) with high electrocatalystic activities in dye-sensitized solar cells. *Catal. Commun.* **2022**, *170*, No. 106497.
(57) Wageh, S.; Al-Ghamdi, A. A.; Jafer, R.; Li, X.; Zhang, P. A new heterojunction in photocatalysis: S-scheme heterojunction. *Chin. J. Catal.* **2021**, *42*, 667−669.
(58) Xu, Q.; Zhang, L.; Cheng, B.; Fan, J.; Yu, J. S-Scheme Heterojunction Photocatalyst. *Chem* **2020**, *6*, 1543−1559.
(59) Zhang, L.; Zhang, J.; Yu, H.; Yu, J. Emerging S-Scheme Photocatalyst. *Adv. Mater.* **2022**, *34*, No. 2107668.

https://doi.org/10.1021/acsomega.2c07899
ACS Omega 2023, 8, 13702−13714

(60) Chen, R.; Xia, J.; Chen, Y.; Shi, H. S-Scheme-Enhanced PMS Activation for Rapidly Degrading Tetracycline Using $CuWO_{4-x}$/$Bi_{12}O_{17}Cl_2$ Heterostructures. *Acta Phys.-Chim. Sin.* **2023**, *39*, 2209012.
(61) Ke, X.; Zhang, J.; Dai, K.; Fan, K.; Liang, C. Integrated S-Scheme Heterojunction of Amine-Functionalized 1D CdSe Nanorods Anchoring on Ultrathin 2D SnNb2O6 Nanosheets for Robust Solar-Driven CO2 Conversion. *Solar RRL* **2021**, *5*, No. 2000805.
(62) Hu, T.; Dai, K.; Zhang, J.; Chen, S. Noble-metal-free Ni2P modified step-scheme SnNb2O6/CdS-diethylenetriamine for photocatalytic hydrogen production under broadband light irradiation. *Appl. Catal., B: Environ.* **2020**, *269*, No. 118844.
(63) Li, X.; Zhang, J.; Huo, Y.; Dai, K.; Li, S.; Chen, S. Two-dimensional sulfur- and chlorine-codoped g-C3N4/CdSe-amine heterostructures nanocomposite with effective interfacial charge transfer and mechanism insight. *Appl. Catal., B: Environ.* **2021**, *280*, No. 119452.
(64) Wang, W.; Zhang, Y.; Chen, Y.; Shi, H. Efficient Degradation of Tetracycline via Coupling of Photocatalysis and Photo-Fenton Processes over a 2D/2D α-Fe2O3/g-C3N4 S-Scheme Heterojunction Catalyst. *Acta Phys.-Chim. Sin.* **2022**, *38*, 2201008.
(65) Fu, J.; Xu, Q.; Low, J.; Jiang, C.; Yu, J. Ultrathin 2D/2D WO_3/g-C_3N_4 step-scheme H_2-production photocatalyst. *Appl. Catal., B* **2019**, *243*, 556−565.
(66) Wu, X.; Zhang, Q.; Su, C. Bi_2MoO_6/Bi_2S_3 S-scheme heterojunction for efficient photocatalytic oxygen evolution. *FlatChem* **2021**, *27*, No. 100244.
(67) Nguyen, V. H.; Pham, A. L. H.; Nguyen, V.-H.; Lee, T.; Nguyen, T. D. Facile synthesis of bismuth(III) based metal-organic framework with difference ligands using microwave irradiation method. *Chem. Eng. Res. Des.* **2022**, *177*, 321−330.
(68) Zahid, A. H.; Han, Q.; Jia, X.; Li, S.; Hangjia, H.; Liu, H. Highly stable 3D multilayered nanoparticles-based β-Bi2O3 hierarchitecture with enhanced photocatalytic activity. *Opt. Mater.* **2020**, *109*, No. 110389.
(69) Hull, S.; Norberg, S. T.; Tucker, M. G.; Eriksson, S. G.; Mohn, C. E.; Stølen, S. Neutron total scattering study of the δ and β phases of Bi 2 O 3. *Dalton Trans.* **2009**, *40*, 8737−8745.
(70) Kahlenberg, V.; Zeiske, T. Structure of γ-Bi2Sn2O7 by high temperature powder neutron diffraction. *Z. Kristallogr.-Cryst. Mater.* **1997**, *212*, 297−301.
(71) Kennedy, B. J.; Elcombe, M. In *Structure and bonding in Bi2Sn2O7*; Materials Science Forum, Trans Tech Publ: 1998; 762−767.
(72) Lannin, J. S.; Calleja, J. M.; Cardona, M. Second-order Raman scattering in the group-Vbsemimetals: Bi, Sb, and As. *Phys. Rev. B* **1975**, *12*, 585.
(73) Gupta, H. C.; Brown, S.; Rani, N.; Gohel, V. B. A lattice dynamical investigation of the Raman and the infrared frequencies of the cubic A2Sn2O7 pyrochlores. *Int. J. Inorg. Mater.* **2001**, *3*, 983−986.
(74) Tan, P. H.; Deng, Y. M.; Zhao, Q. Temperature-dependent Raman spectra and anomalous Raman phenomenon of highly oriented pyrolytic graphite. *Phys. Rev. B* **1998**, *58*, 5435−5439.
(75) Prasad, N.; Balasubramanian, K. Raman spectral probe on increased local vibrational modes and phonon lifetimes in Ho3+ doped Bi2O3 micro-rods. *J. Raman Spectrosc.* **2016**, *47*, 1266−1270.
(76) Fan, H.; Wang, G.; Hu, L. Infrared, Raman and XPS spectroscopic studies of Bi2O3−B2O3−Ga2O3 glasses. *Solid State Sci.* **2009**, *11*, 2065−2070.
(77) Lu, X.; Che, W.; Hu, X.; Wang, Y.; Zhang, A.; Deng, F.; Luo, S.; Dionysiou, D. D. The facile fabrication of novel visible-light-driven Z-scheme $CuInS_2/Bi_2WO_6$ heterojunction with intimate interface contact by in situ hydrothermal growth strategy for extraordinary photocatalytic performance. *Chem. Eng. J.* **2019**, *356*, 819−829.
(78) Zhang, H.; He, J.; Zhai, C.; Zhu, M. 2D Bi_2WO_6/MoS_2 as a new photo-activated carrier for boosting electrocatalytic methanol oxidation with visible light illumination. *Chin. Chem. Lett.* **2019**, *30*, 2338−2342.
(79) Shen, J.-C.; Zeng, H.-Y.; Chen, C.-R.; Xu, S. Novel plasmonic p-n heterojunction Ag-$Ag_2CO_3/Bi_2Sn_2O_7$ photocatalyst for Cr(VI) reduction. *J. Taiwan Inst. Chem. Eng.* **2021**, *120*, 106−115.
(80) Jiang, L.; Xie, Y.; He, F.; Ling, Y.; Zhao, J.; Ye, H.; Li, S.; Wang, J.; Hou, Y. Facile synthesis of GO as middle carrier modified flower-like BiOBr and C_3N_4 nanosheets for simultaneous treatment of chromium(VI) and tetracycline. *Chin. Chem. Lett.* **2021**, *32*, 2187−2191.
(81) Nie, H.; Wei, K.; Li, Y.; Liu, Y.; Zhao, Y.; Huang, H.; Shao, M.; Liu, Y.; Kang, Z. Carbon dots/Bi_2WO_6 composite with compensatory photo-electronic effect for overall water photo-splitting at normal pressure. *Chin. Chem. Lett.* **2021**, *32*, 2283−2286.
(82) Wu, C.; Shen, Q.; Liu, J.; Jiang, L.; Sheng, J.; Li, Y.; Yang, H. Regulation of charge transfer in ZnO/$Bi_2Sn_2O_7$ heterojunction for enhanced photocatalytic performance towards antibiotic degradation. *J. Photochem. Photobiol. A Chem.* **2022**, *433*, No. 114142.
(83) Liu, X.; Kang, Y.; Wang, Y. Novel high-efficiency visible-light-driven p-n heterojunction β-Bi_2O_3/Ag_2WO_4 photocatalysts. *Chem. Phys. Lett.* **2022**, *790*, No. 139347.
(84) Meng, Q.; Yin, Z.; Lu, Q.; Xia, Y.; Zhao, Y.; Wan, X. Self-assembled $BiFeO_3/\beta$-Bi_2O_3 heterojunction nanofibers with enhanced visible-light-driven photocatalytic denitrification properties. *Mater. Lett.* **2022**, *309*, No. 131402.
(85) Wu, Y.; Yue, Z.; Liu, A.; Yang, P.; Zhu, M. P-Type Cu-Doped $Zn_{0.3}Cd_{0.7}S$/Graphene Photocathode for Efficient Water Splitting in a Photoelectrochemical Tandem Cell. *ACS Sustainable Chem. Eng.* **2016**, *4*, 2569−2577.
(86) Yu, B.; Wu, Y.; Meng, F.; Wang, Q.; Jia, X.; Wasim Khan, M.; Huang, C.; Zhang, S.; Yang, L.; Wu, H. Formation of hierarchical Bi_2MoO_6/ln_2S_3 S-scheme heterojunction with rich oxygen vacancies for boosting photocatalytic CO2 reduction. *Chem. Eng. J.* **2022**, *429*, No. 132456.
(87) Li, S.; Wang, C.; Cai, M.; Yang, F.; Liu, Y.; Chen, J.; Zhang, P.; Li, X.; Chen, X. Facile fabrication of TaON/Bi_2MoO_6 core−shell S-scheme heterojunction nanofibers for boosting visible-light catalytic levofloxacin degradation and Cr(VI) reduction. *Chem. Eng. J.* **2022**, *428*, No. 131158.
(88) Heidari, S.; Haghighi, M.; Shabani, M. Ultrasound assisted dispersion of $Bi_2Sn_2O_7$-C_3N_4 nanophotocatalyst over various amount of zeolite Y for enhanced solar-light photocatalytic degradation of tetracycline in aqueous solution. *Ultrason. Sonochem.* **2018**, *43*, 61−72.
(89) Ding, S.; Dong, T.; Peppel, T.; Steinfeldt, N.; Hu, J.; Strunk, J. Construction of amorphous SiO_2 modified β-Bi_2O_3 porous hierarchical microspheres for photocatalytic antibiotics degradation. *J. Colloid Interface Sci.* **2022**, *607*, 1717−1729.
(90) Huang, S.; Zhang, J.; Qin, Y.; Song, F.; Du, C.; Su, Y. Direct Z-scheme $SnO_2/Bi_2Sn_2O_7$ photocatalyst for antibiotics removal: Insight on the enhanced photocatalytic performance and promoted charge separation mechanism. *J. Photochem. Photobiol. A Chem.* **2021**, *404*, No. 112947.
(91) Gao, Q.; Sun, K.; Cui, Y.; Wang, S.; Liu, C.; Liu, B. In situ growth of 2D/3D Bi_2MoO_6/CeO_2 heterostructures toward enhanced photodegradation and Cr(VI) reduction. *Sep. Purif. Technol.* **2022**, *285*, No. 120312.
(92) Peng, P.; Chen, Z.; Li, X.; Wu, Y.; Xia, Y.; Duan, A.; Wang, D.; Yang, Q. Biomass-derived carbon quantum dots modified Bi_2MoO_6/Bi_2S_3 heterojunction for efficient photocatalytic removal of organic pollutants and Cr (VI). *Sep. Purif. Technol.* **2022**, *291*, No. 120901.
(93) Guo, F.; Chen, Z.; Huang, X.; Cao, L.; Cheng, X.; Shi, W.; Chen, L. Ternary Ni_2P/Bi_2MoO_6/g-C_3N_4 composite with Z-scheme electron transfer path for enhanced removal broad-spectrum antibiotics by the synergistic effect of adsorption and photocatalysis. *Chin. J. Chem. Eng.* **2022**, *44*, 157−168.
(94) Tang, D.; Chen, X.; Yan, J.; Xiong, Z.; Lou, X.; Ye, C.; Chen, J.; Qiu, T. Facile one-pot synthesis of a BiOBr/Bi_2WO_6 heterojunction with enhanced visible-light photocatalytic activity for tetracycline degradation. *Chin. J. Chem. Eng.* **2023**, *53*, 222−231.

https://doi.org/10.1021/acsomega.2c07899
ACS Omega 2023, 8, 13702−13714

(95) Tao, R.; Shao, C.; Li, X.; Li, X.; Liu, S.; Yang, S.; Zhao, C.; Liu, Y. Bi_2MoO_6/$BiFeO_3$ heterojunction nanofibers: Enhanced photocatalytic activity, charge separation mechanism and magnetic separability. *J. Colloid Interface Sci.* **2018**, *529*, 404−414.
(96) Yang, H.; Zhang, J. F.; Dai, K. Organic amine surface modified one-dimensional CdSe0.8S0.2-diethylenetriamine/two-dimensional SnNb2O6 S-scheme heterojunction with promoted visible-light-driven photocatalytic CO2 reduction. *Chin. J. Catal.* **2022**, *43*, 255−264.
(97) Li, X.; Wang, Z.; Zhang, J.; Dai, K.; Fan, K.; Dawson, G. Branch-like CdxZn1-xSe/Cu2O@Cu step-scheme heterojunction for CO2 photoreduction. *Mater. Today Phys.* **2022**, *26*, No. 100729.
(98) Dai, K.; Lv, J.; Zhang, J.; Zhu, G.; Geng, L.; Liang, C. Efficient Visible-Light-Driven Splitting of Water into Hydrogen over Surface-Fluorinated Anatase TiO2 Nanosheets with Exposed {001} Facets/Layered CdS−Diethylenetriamine Nanobelts. *ACS Sustainable Chem. Eng.* **2018**, *6*, 12817−12826.
(99) Zhao, X.; Lu, Z.; Wei, M.; Zhang, M.; Dong, H.; Yi, C.; Ji, R.; Yan, Y. Synergetic effect of carbon sphere derived from yeast with magnetism and cobalt oxide nanochains towards improving photodegradation activity for various pollutants. *Appl. Catal., B: Environ.* **2018**, *220*, 137−147.
(100) Wang, J.; Zhi, D.; Zhou, H.; He, X.; Zhang, D. Evaluating tetracycline degradation pathway and intermediate toxicity during the electrochemical oxidation over a Ti/Ti_4O_7 anode. *Water Res.* **2018**, *137*, 324−334.
(101) Li, S.; Wang, C.; Liu, Y.; Xue, B.; Jiang, W.; Liu, Y.; Mo, L.; Chen, X. Photocatalytic degradation of antibiotics using a novel Ag/Ag_2S/Bi_2MoO_6 plasmonic p-n heterojunction photocatalyst: Mineralization activity, degradation pathways and boosted charge separation mechanism. *Chem. Eng. J.* **2021**, *415*, No. 128991.
(102) Ye, Z.; Li, J.; Zhou, M.; Wang, H.; Ma, Y.; Huo, P.; Yu, L.; Yan, Y. Well-dispersed nebula-like ZnO/CeO_2@HNTs heterostructure for efficient photocatalytic degradation of tetracycline. *Chem. Eng. J.* **2016**, *304*, 917−933.
(103) Hu, Y.; Chen, D.; Zhang, R.; Ding, Y.; Ren, Z.; Fu, M.; Cao, X.; Zeng, G. Singlet oxygen-dominated activation of peroxymonosulfate by passion fruit shell derived biochar for catalytic degradation of tetracycline through a non-radical oxidation pathway. *J. Hazard. Mater.* **2021**, *419*, No. 126495.
(104) Shi, W.; Shu, K.; Sun, H.; Ren, H.; Li, M.; Chen, F.; Guo, F. Dual enhancement of capturing photogenerated electrons by loading CoP nanoparticles on N-deficient graphitic carbon nitride for efficient photocatalytic degradation of tetracycline under visible light. *Sep. Purif. Technol.* **2020**, *246*, No. 116930.
(105) Liu, K.; Zhang, H.; Fu, T.; Wang, L.; Tang, R.; Tong, Z.; Huang, X. Construction of BiOBr/Ti_3C_2/exfoliated montmorillonite Schottky junction: New insights into exfoliated montmorillonite for inducing MXene oxygen functionalization and enhancing photocatalytic activity. *Chem. Eng. J.* **2022**, *438*, No. 135609.
(106) Zhao, C.; Li, Y.; Chu, H.; Pan, X.; Ling, L.; Wang, P.; Fu, H.; Wang, C.-C.; Wang, Z. Construction of direct Z-scheme Bi_5O_7I/UiO-66-NH_2 heterojunction photocatalysts for enhanced degradation of ciprofloxacin: Mechanism insight, pathway analysis and toxicity evaluation. *J. Hazard. Mater.* **2021**, *419*, No. 126466.
(107) Wu, Y.; Zhao, X.; Huang, S.; Li, Y.; Zhang, X.; Zeng, G.; Niu, L.; Ling, Y.; Zhang, Y. Facile construction of 2D g-C_3N_4 supported nanoflower-like $NaBiO_3$ with direct Z-scheme heterojunctions and insight into its photocatalytic degradation of tetracycline. *J. Hazard. Mater.* **2021**, *414*, No. 125547.
(108) Wang, Y.; Wang, K.; Wang, J.; Wu, X.; Zhang, G. Sb2WO6/BiOBr 2D nanocomposite S-scheme photocatalyst for NO removal. *J. Mater. Sci. Technol.* **2020**, *56*, 236−243.
(109) Ren, Y.; Li, Y.; Wu, X.; Wang, J.; Zhang, G. S-scheme Sb2WO6/g-C3N4 photocatalysts with enhanced visible-light-induced photocatalytic NO oxidation performance. *Chin. J. Catal.* **2021**, *42*, 69−77.
(110) Wang, C.; Liu, H.; Wang, G.; Fang, H.; Yuan, X.; Lu, C. Photocatalytic removal of metronidazole and Cr (VI) by a novel $Zn_3In_2S_6$/Bi_2O_3 S-scheme heterojunction: Performance, mechanism insight and toxicity assessment. *Chem. Eng. J.* **2022**, *450*, No. 138167.
(111) Zhang, Z.; Pan, Z.; Guo, Y.; Wong, P. K.; Zhou, X.; Bai, R. In-situ growth of all-solid Z-scheme heterojunction photocatalyst of $Bi_7O_9I_3$/g-C_3N_4 and high efficient degradation of antibiotic under visible light. *Appl. Catal., B* **2020**, *261*, No. 118212.
(112) Zhang, X.; Zhang, H.; Yu, J.; Wu, Z.; Zhou, Q. Preparation of flower-like Co_3O_4 QDs/Bi_2WO_6 p-n heterojunction photocatalyst and its degradation mechanism of efficient visible-light-driven photocatalytic tetracycline antibiotics. *Appl. Surf. Sci.* **2022**, *585*, No. 152547.
(113) Lu, C.; Wang, L.; Yang, D.; Jin, Z.; Wang, X.; Xu, J.; Li, Z.; Shi, W.; Guan, W.; Huang, W. Boosted tetracycline and Cr(VI) simultaneous cleanup over Z-Scheme $BiPO_4$/$CuBi_2O_4$ p-n heterojunction with 0D/1D trepang-like structure under simulated sunlight irradiation. *J. Alloys Compd.* **2022**, *919*, No. 165849.
(114) Li, W.; Wang, Z.; Li, Y.; Ghasemi, J. B.; Li, J.; Zhang, G. Visible-NIR light-responsive 0D/2D CQDs/Sb2WO6 nanosheets with enhanced photocatalytic degradation performance of RhB: Unveiling the dual roles of CQDs and mechanism study. *J. Hazard. Mater.* **2022**, *424*, No. 127595.
(115) Wang, X.; Ren, Y.; Li, Y.; Zhang, G. Fabrication of 1D/2D BiPO4/g-C3N4 heterostructured photocatalyst with enhanced photocatalytic efficiency for NO removal. *Chemosphere* **2022**, *287*, No. 132098.

https://doi.org/10.1021/acsomega.2c07899
ACS Omega 2023, 8, 13702−13714